A functional tool to explore the reliability of micro-earthquake focal mechanism solution for seismotectonic purposes

Guido Maria Adinolfi [1, 3, *], Raffaella De Matteis [1], Rita de Nardis [2, 3] and Aldo Zollo [4]

[1] Dipartimento di Scienze e Tecnologie, Università degli Studi del Sannio, via De Sanctis, 82100 Benevento, Italy

[2] Dipartimento di Scienze Psicologiche, della Salute e del Territorio, Università di Chieti-Pescara "G. d'Annunzio", via dei Vestini, 32, 66100, Chieti, Italy

[3] CRUST Centro inteRUniversitario per l'analisi SismoTettonica tridimensionale, Italy

[4] Dipartimento di Fisica, Università di Napoli "Federico II", Complesso Universitario di Monte S.Angelo, via Cinthia, 80124 Napoli, Italy

* Corresponding author: gmadinolfi@unisannio.it

ABSTRACT

Improving the knowledge of seismogenic faults requires the integration of geological, seismological, and geophysical information. Among several analyses, the definition of earthquake focal mechanisms plays an essential role in providing information about the geometry of individual faults and the stress regime acting in a region. Fault plane solutions can be retrieved by several techniques operating in specific magnitude ranges, both in the time and frequency domain and using different data.
For earthquakes of low magnitude, the limited number of available data and their uncertainties can compromise the stability of fault plane solutions. In this work, we propose a useful methodology to evaluate how well a seismic network, used to monitor natural and/or induced micro-seismicity, estimates focal mechanisms as a function of magnitude, location, and kinematics of seismic source and consequently their reliability in defining seismotectonic models. To study the consistency of focal mechanism solutions, we use a Bayesian approach that jointly inverts the P/S long-period spectral-level ratios and the P polarities to infer the fault-plane solutions. We applied this methodology, by computing synthetic data, to the local seismic network operating in the Campania-Lucania Apennines (Southern Italy) aimed to monitor the complex normal fault system activated during the Ms 6.9, 1980 earthquake. We demonstrate that the method we propose is effective and can be adapted for other case studies with a double purpose. It can be a valid tool to design or to test the performance of local seismic networks and more generally it can be used to assign an absolute uncertainty to focal mechanism solutions fundamental for seismotectonic studies.

INTRODUCTION

Fault plane solutions represent primary information to describe earthquakes. The assessment of earthquake location, magnitude, and focal mechanism are the fundamental operations to characterize the earthquake source using a point source approximation. The focal mechanism describes the basic geometry and kinematics of a point source in terms of strike, dip, and rake of the fault plane along which the earthquake occurred. So, the focal mechanism is the most important marker of the geometry of the seismogenic faults and their style of faulting. Moreover, seismicity and focal mechanisms of events are often used to constrain seismotectonic models, individual seismogenic sources, the regional strain, and stress fields, also for small magnitudes. Consequently, an evaluation of their effective reliability becomes a fundamental issue in seismotectonic studies.

Nevertheless, focal mechanisms cannot be calculated and constrained every time an earthquake occurs. Although the calculation of focal mechanisms represents a routine analysis for seismological agencies, the solutions are calculated only for a specific range of magnitudes, usually greater than 4. In fact, constraining the solution for earthquakes with small magnitude is still a challenge, despite the advancement in the technological process and the use of increasingly performing seismic networks. This is due to several factors that we will analyse in detail. The techniques used to define the focal mechanism of large to moderate earthquakes are based on the inversion of the moment tensor, which corresponds to a stable and robust procedure, so much that it is the most common method for this type of analysis (Dreger, 2003; Delouis, 2014; Sokos and Zahradnik, 2013; Cesca et al., 2011). This technique requires accurate knowledge of the propagation medium in relation to the range of frequencies used for the modelling waveforms recorded during an earthquake. The smaller an earthquake, the higher the frequency range of the signal to be modelled, the more detailed the knowledge and scale of the Earth's interior must be. Several methods have been proposed to achieve a stable inversion of the moment tensor for earthquakes with a magnitude less than 3. Hybrid approaches that invert both amplitude and waveform moment tensor use the principal component

analysis of seismograms (Vavrycuk et al., 2017) or moment tensor refinement techniques (Kwiatek et al. 2016; Bentz at al., 2018) to facilitate a robust determination of the source type and its kinematics. In particular, the retrieved moment tensor is typically decomposed into volumetric and deviatoric components. Constraining the earthquake as a double-couple source can erroneously affect the retrieved fault plane solutions, especially in the case of induced seismicity where the volumetric or non-double couple component must be considered (Kwiatek et al. 2016).

Other analytical techniques are based on the recognition of the source radiation pattern. According to the position of seismic stations relative to the source, seismic waves on seismograms show different amplitudes and polarities. These features can constrain the geometry of the earthquake faulting through estimating the angular parameters strike, dip, and rake. The classical method (Raesenberg and Oppenheimer, 1985;) uses the P-wave polarities; more advanced approaches better constrain the focal mechanism of small earthquakes using P- or S- wave amplitudes or amplitude ratios together with first motions (Snoke, 2003). In fact, the use of polarities alone is inappropriate, especially if we consider micro-seismicity ($M < 3$). The reasons could be the limited number of available data, their uncertainties, and the difficulty of measuring the P-polarity with a sufficient degree of precision. For these reasons, different techniques using different types of measurements such as P-wave amplitudes (Julian and Foulger, 1996; Tarantino et al., 2019), P/S or S/P amplitude ratios measured in the time or the frequency domain (Kisslinger et al., 1981; Rau et al., 1996; Hardebeck and Shearer, 2003; De Matteis et al., 2016), or S-wave polarizations (Zollo and Bernard, 1991) have been developed. The joint inversion of polarities and amplitude ratios led to more stable and robust solutions, allowing to account for geological site effects and to decrease the effects produced by the geometric and anelastic attenuations.

Two kinds of errors generally influence the goodness of the solution and retrieved model (Michele et al., 2016): the perturbation errors that are related to how the uncertainty on data affects the model, and the resolution errors that are referred to the capability to retrieve a correct model, given a dataset as input or how accurate could be the model that we can recover, even with error-free data. The sum

93 of perturbation and resolution errors corresponds to the final errors on the model obtained by solving

94 an inverse problem, as the solution of focal mechanism. In particular, the resolution errors depend on

95 the available data, and so on the initial condition of the inverse problem. In the case of focal mechanism,

96 the number of seismic stations, as well as the seismic network geometry, and the velocity structure of

97 the crust influence the resolution and the reliability of the retrieved model.

98 How will the geometry of a seismic network determine the accuracy of focal mechanism solutions? The

99 answer to this question requires a deep knowledge of the geophysical and geological characteristics of

100 the region, often unavailable. Moreover, the theoretical relationships that predict the focal mechanism

101 solutions for an earthquake scenario could be very complicated if several factors, such as network

102 configuration, noise level, source magnitude, or source kinematics are taken into account. A network

103 configuration may be optimal for earthquake locations, but not for retrieving fault plane solutions (Hardt

104 and Scherbaum, 1994). In fact, a given geometry may resolve some fault kinematics better than others.

105 A seismic network layout is strictly associated with the goals of the network and the available funds;

106 according to these features, a network operator decides how many stations are required and where

107 they should be located (Havskov et al.; 2011). So, the number of seismic stations, the size, and geometry

108 of the network are defined after a preliminary phase based on the evaluation of the specific

109 seismological target (Trnkoczy et al., 2009; Hardt and Scherbaum 1994; Steinberg et al. 1995; Bartal

110 et al. 2000). In the case of small earthquakes, the available recordings come from only a portion of the

111 total network, while the distant stations show a seismic signal buried inside the noise. In order to detect

112 and locate low-magnitude earthquakes, we must increase the number of seismic stations for area units

113 by building a dense seismic network.

114 In this study, we propose a useful tool to evaluate both 1) the reliability of focal mechanism solutions

115 inferred by the inversion of different seismological data and 2) the performance of the seismic network

116 to assess focal mechanism solutions and their errors. We evaluate the network capability to solve focal

117 mechanisms as a function of magnitude, location, and kinematics of seismic source. We consider three

118 synthetic data set: P-wave polarities, P- S-wave amplitude spectral ratios and polarities and amplitude

119 ratios together. Moreover, different levels of noise are considered in order to simulate more realistic

120 conditions.

121 We selected as target the Irpinia Seismic Network (ISNet), a local seismic network that monitors the

122 Irpinia complex normal fault system (Southern Italy), activated during the Ms 6.9 earthquake of 23rd

123 November 1980. Evaluating the specific performance of an existing network for a seismological goal is

124 critical and can be used to decide how to improve its layout.

125

METHODOLOGY

127 With the main aim to define the reliability of focal mechanisms retrieved by specific seismic networks,

128 we propose a methodology based on an empirical approach that consists of different steps.

129 *Configuration and Parameter Tuning (Step 1).* In a preliminary phase, we select for each earthquake

130 simulation the: a) fault plane solution to test, b) seismic observables to be computed (i.e. P-wave

131 polarities or P- S-wave amplitude spectral ratios), c) magnitude, d) the earthquake epicentre and depth;

132 e) the network geometry; f) the noise level. The fault plane solution to test can be derived from

133 instrumental seismicity as one of the strongest earthquakes occurred in the area or a median solution

134 of the available ones or simply a fault plane solution representative of the regional seismotectonic.

135 Once the network geometry and the hypocentre of the earthquake are defined, the seismic stations

136 (number and type) for which the synthetic data are computed must be selected. The number of seismic

137 stations that record an event depends on earthquake magnitude, source-stations distance, crustal

138 medium properties, and the level of noise. We use an empirical approach, based on the statistical

139 analysis of the local seismicity catalog, that allows us to define, for each magnitude range, a maximum

140 (threshold) epicentral distance for which only the seismic stations within this distance are considered

141 (See data analysis).

142 *Synthetic Data Computation (Step 2).* Using a crustal velocity model and the source-receiver relative

143 position, the synthetic data are computed for the theoretical fault plane solution. The seismic

144   observables that can be reproduced are a) P-wave polarities, b) P/S spectral amplitude ratios, and c)

145   polarities and amplitude ratios together. For the P/S spectral level ratios, the Gaussian noise level is

146   added.

147   *Focal Mechansim Inversion (Step 3).* We estimated focal mechanism using BISTROP code (De Matteis

148   et al., 2016) that jointly inverts the ratio between the P- and S-wave long-period spectral levels and

149   the P-wave polarities according to a Bayesian approach. BISTROP has the advantage to use different

150   observables for the determination of fault plane solutions, such as the P/S long-period spectral level

151   ratios or P-wave polarities, individually or together. The benefits of the use of spectral level ratios are

152   multiples: 1) they can be measured for a broad range of magnitudes (also for M < 3; De Matteis et al.,

153   2016); 2) they can be calculated by automatic procedures without visual inspection; 3) their estimates

154   do not require to identify the first arrival time accurately, but only a time window of signal containing

155   P- or S-phase is mandatory and 4) the spectral amplitude ratios, they can generally be used without

156   the exact knowledge of the geological soil conditions (site effects) and geometric/anelastic attenuation.

157   Moreover, the joint inversion of amplitude spectral ratios and polarities led to constraining fault plane

158   solutions reducing the error associated with the estimates of retrieved parameters. BISTROP solves an

159   inverse problem through a probabilistic formulation leading to a complete representation of uncertainty

160   and correlation of the inferred parameters.

161   For a double-couple seismic source, the radiation pattern depends on fault kinematics and relative

162   source-station position. In fact, it can be represented as a function of 1) strike, dip and rake angles (φ,

163   δ, λ) and 2) take-off and azimuth angles (i_h, φ_r). We can define the ratio between P- and S-wave

164   radiation pattern coefficients as:

165
$$\frac{\mathcal{R}^P\left(\phi,\delta,\lambda,i_h,\phi_R\right)}{\mathcal{R}^S\left(\phi,\delta,\lambda,i_h,\phi_R\right)} = \left(\frac{\alpha_s^2 \alpha_r}{\beta_s^2 \beta_r}\right) \ \frac{\Omega_0^P}{\Omega_0^S} \tag{1}$$

166   where Ω_0^P and Ω_0^S are the long-period spectral level of the P- and S-waves, respectively, and α_s, α_r,

167   β_s, β_r, are the P- and S-wave velocities at the source and at the receiver, respectively. Thus, using the

168   displacement spectra, assuming a given source and attenuation model (Boatwright,1980), we can derive

from the signal recorded by a seismic station the ratio of radiation pattern coefficients for P- and S-phases, as well as $\alpha, \beta, i_h, \varphi_r$ are known from the earthquake location and the velocity model used. So, from a theoretical point of view, the spectral amplitude ratios measured at several seismic stations can be used to retrieve the ratio of radiation pattern coefficients $\mathcal{R}^P_{\theta\varphi}/\mathcal{R}^S_{\theta\varphi}$ as a function of the source-receiver azimuth and take-off angles.

BISTROP jointly inverts the spectral amplitude ratios with the observed P-wave polarities to infer the parameters φ, δ, λ of the focal mechanism in a Bayesian framework. A posterior probability density function (PDF), for the vector of model parameter $\boldsymbol{m}$ (φ, δ, λ) and the vector of observed data $\boldsymbol{d}$, is defined as:

$$q(\boldsymbol{m}|\boldsymbol{d}) = \frac{f(\boldsymbol{d}|\boldsymbol{m})p(\boldsymbol{m})}{\int_M f(\boldsymbol{d}|\boldsymbol{m}')p(\boldsymbol{m}')\,d\boldsymbol{m}'} \qquad (2)$$

where $f(\mathbf{d}|\mathbf{m})$ is the conditional probability function that represents the PDF given the data $\mathbf{d}$ and for parameter vector $\boldsymbol{m}$ in the model parameter space M, and $p(\boldsymbol{m})$ is the a priori PDF. If P-wave polarities and P/S spectral level ratios are independent datasets, the conditional probability function may be written as:

$$f(\mathbf{d}|\mathbf{m}) = f(\boldsymbol{d}^L|\mathbf{m})f(\boldsymbol{d}^P|\mathbf{m}). \qquad (3)$$

in which the pdf of the data vector $\boldsymbol{d}^L$ of N^L measurements of spectral ratios is multiplied for the pdf of data vector $\boldsymbol{d}^P$ of N^P measurements of P-wave polarities given the model $\boldsymbol{m}$.

Assuming that the observables have the same finite variance, for the N^L observations of spectral level ratios the conditional probability function may be defined as:

$$f(\boldsymbol{d}^L|\boldsymbol{m}) = \frac{1}{\left(\sqrt{2\pi}\sigma\ \right)^{N_L}} exp\left(-\frac{\sum_{i=1}^{N_L}\{d_i - [G(\boldsymbol{m})]_i\}^2}{2\sigma^2}\right) \tag{4}$$

Where $G(\boldsymbol{m})$ represents a functional relationship between model and data and corresponds to Equation 1 and σ represents the uncertainty on the spectral measure.

For the N^P observations of P-wave polarities, the conditional probability function is (Brillinger et al., 1980):

$$f(\boldsymbol{d}^P|\boldsymbol{m}) = \prod_{i=1}^{N_P}\frac{1}{2}[1 + \psi(\mathcal{R}_i^P,\gamma_i,\rho_0)Y_i sign(\mathcal{R}_i^P)] \tag{5}$$

in which:

.

$$\psi(\mathcal{R}_i^P,\gamma_i,\rho_0) = (1 - 2\gamma_i)\,\mathrm{erf}\left(\left|\rho_0\mathcal{R}_i^P(\boldsymbol{m})\right|\right) \tag{6}$$

The quantity reported in square brackets in Equation 5 represents the probability that the observed i_{th} polarity γ_i is consistent with the theoretical one computed from the model $\boldsymbol{m}$, whose theoretical P-wave amplitude is $\mathcal{R}_i^P$ and $sign(\mathcal{R}_i^P)$ is its polarity at i_{th} station for a given fault plane solution. The parameters ρ_s and γ_0 , referring to the errors in ray tracing due to velocity model ambiguity and to the uncertainty on polarity reading, regulating the shape of the PDF. For more details about the mathematical formulation, see De Matteis et al. (2016).

Evaluation of the Results (Step 4). Once the best solution is estimated, the focal mechanism uncertainties and its misfit, respect to the theoretical solution as Kagan angle, are computed. The focal mechanism parameter (strike, dip and rake) misfit and their uncertainties are also calculated.

IRPINIA SEISMIC NETWORK

As testing case of our methodology, we choose the area of the M 6.9, 1980 Irpinia earthquake (Southern Italy). Since 2005, ISNet, a local, dense seismic network monitors the seismicity along the Campania-Lucania Apennines covering an area of about 100 × 70 km^2 (Figure 1; Weber et al., 2007). The seismic stations are deployed within an elliptic area whose major axis, parallel to the Apennine chain, has a NW-SE trend with an average inter-stations distance of 15 km that reaches 10 km in the inner central zone. Each seismic station ensures a high dynamic range and it is equipped with a strong-motion accelerometer, Guralp CMG-5T or Kinemetrics Episensor, and a short period three-component seismometer, Geotech S13-J with a natural period of 1 sec. In 6 cases, broadband seismometers are installed such as the Nanometrics Trillium with a flat response in the range 0.025–50 Hz. ISNet is operating by INFO (Irpinia Near Fault Observatory) and it provides real-time data at local control centres for earthquake early warning systems or real-time seismic monitoring (Satriano et al., 2011). Seismic events are automatically identified and located from continuous recordings by automatic Earth-worm Binder and data are then manually revised by operators (Festa et al., 2020).

The 1980, M 6.9, Irpinia earthquake was one of the most destructive, instrumental earthquakes of the Southern Apennines, causing about 3000 fatalities and severe damages in the Campania and Basilicata regions. It activated a NW-SE trending normal fault system with a complex rupture process involving multiple fault segments according to (at least) three different nucleation episodes delayed each other of 20 s (Bernard and Zollo, 1989; Pantosti and Valensise; 1993; Amoruso et al.; 2005). No large earthquakes occurred in the Irpinia region since 1980. A Mw 4.9 earthquake took place in 1996 originating a seismic sequence inside the epicentral area of the 1980 earthquake (Figure 1; Cocco et al., 1999). Recent instrumental seismicity occurs mainly in the first 15 km of the crust showing fault plane solutions with normal and normal-strike slip kinematics, indicating a dominant SW-NE extensional regime (Pasquale et al., 2009; De Matteis et al., 2012; Bello et al., 2021). Low-magnitude seismicity (M_L < 3.6) is spread into a large volume related to the activity of major fault segments of the 1980

238   Irpinia earthquake (Figure 1; Adinolfi et al., 2019; Adinolfi et al., 2020). Seismic sequences or swarms

239   often occurred in the area, extremely clustered in time (from several hours to a few days) and space

240   and seem to be controlled by high pore fluid pressure of saturated Apulian carbonates bounded by

241   normal seismogenic faults (Stabile et al., 2012; Amoroso et al, 2014).

242

243   **DATA ANALYSIS**

244   We applied the method we proposed and evaluated the capability of the ISNet local network to resolve

245   fault plane solutions using different observables as input data: a) P-wave polarities, b) P/S spectral

246   amplitude ratios and c) polarities and amplitude ratios together. the analysis is carried out by evaluating

247   the effect of 1) earthquake magnitude, 2) epicentral location, 3) earthquake depth, 4) signal-to-noise

248   ratio, and 5) fault kinematics on retrieved focal solutions as previously described.

249   *Step 1*. In order to selectfocal mechanisms (FMs) to be used for our resolution study (Figure 2a), we

250   carried out statistical analysis to define the most frequent fault plane solutions of instrumental

251   seismicity. We classified, according to the plunge of P- and T-axes, the fault plane solutions reported

252   in De Matteis et al. (2012) choosing only the FMs occurring within the Irpinia area since 2005 to 2011.

253   As shown in Figure 2b, splitting the range of the data into equal-sized bins, we selected the focal

254   mechanism corresponding to the median value of the most populated class. We report it in Figure 2a

255   as FM2. This corresponds to a normal-strike-slip fault plane solution with strike, dip, and rake equal to

256   292°, 53°, and -133°, respectively. Then, we decided to test the focal mechanism solution of the1980

257   Irpinia earthquake, a pure normal fault (strike, dip, rake: 317°, 59°, -85°; Westaway and Jackson, 1987;

258   Fig. 2a) here and after FM1. This solution is very similar to the focal mechanism corresponding to: 1)

259   the regional stress field (see Supplementary Material); 2) the M_L 2.9, Laviano earthquake, one of the

260   most energetic earthquakes of the last years (Stabile et al.; 2012), and 3) those of the 2nd, 3rd, 4th most

261   populated bins. Finally, we selected the solution corresponding to the 5th bin reported as FM3 in Figure

262   2a. This focal mechanism is quite different from the others due to a predominant component along the

263   fault strike (strike, dip, rake: 274°, 71°, -128°)

264   *Step 2.* For each of the three selected fault plane kinematics, we calculated synthetic data (P-wave

265   polarities or P- and S-wave spectral amplitudes) at seismic stations varying the earthquake location and

266   by using a local velocity model (Matrullo et al., 2013). We discretize the study area with a square grid

267   (100 X 100 km^2), centred on the barycentre of ISNet, with 441 nodes and a sampling step of 5 km.

268   Each node corresponds to a possible earthquake epicentre (Figure 3).

269   For each grid node and according to the earthquake magnitude to be tested, we have to select the

270   ISNet stations for simulations. The number of seismic stations that record an event depends on

271   earthquake magnitude, source-stations distance, crustal medium properties, and the noise level.

272   Theoretical relationships that link the seismic source to the signal recorded at every single station are

273   quite complicated (Kwiatek et al., 2016; 2020) and are based on the accurate knowledge of crustal

274   volumes in which the seismic waves propagated, such as the three-dimensional wave velocity structure,

275   anelastic attenuation or/and site conditions of a single receiver. To overcome this limitation, we used

276   an empirical approach to define the number and the distance of the seismic stations that record a

277   seismic signal as a function of magnitude, once its epicentral location (grid node) and depth are fixed.

278   Using the bulletin data retrieved by INFO at ISNet during the last two years (January 2019-March 2021;

279   http://isnet-bulletin.fisica.unina.it/cgi-bin/isnet-events/isnet.cgi), we selected two earthquake catalog

280   datasets with depths equal to 5 (+- 2) km and 10 (+- 2) km, respectively, and local magnitude ranging

281   between 1.0 and 2.5. These choices are motivated by the characteristics of the Irpinia micro-seismicity

282   recorded by ISNet. Then, we divided each dataset into bins of 0.5 magnitudes and for each bin, we

283   retrieved the median number of P-wave polarity readings and the median epicentral distance of the

284   farthest station that recorded the earthquake (Table 1). The bulletin data are manually revised by

285   operators, and we selected only seismic records that provide P- and/or S- wave arrival times. The

286   median value of the distance of the farthest station is then used to select the seismic stations for which

287   synthetic data are calculated. Therefore, for each earthquake simulation of specific magnitude and

288   depth, only the seismic stations with a distance, from the grid node under examination (epicentre), equal

289   or lower than the maximum distance, reported in Table 1, are considered. We run simulations only for

290   earthquakes recorded at least by 6 seismic stations. The synthetic P-wave polarities are simulated only

291   at a number of stations corresponding to the median value previously defined. (Table 1). We pointed

292   out that the number of P-wave polarities empirically assigned is related to the available earthquake

293   catalogue data of the Irpinia region where the seismicity can occur in different portions of the area

294   covered by the network, not always with optimal azimuthal coverage.

295   Additionally, we simulated the uncertainty on the measure of spectral level ratios or the effect of seismic

296   noise adding a zero mean, Gaussian noise to the synthetic data with a standard deviation equal to two

297   different percentage levels, as 5% and 30%. With this configuration, we simulated:

298   • Three datasets of seismic observables: P-wave polarities (D1), P/S spectral level ratios (D2) and

299   polarities and P/S spectral level ratios together (D3)

300   • Two hypocentre depths: 5 km and 10 km

301   • Three magnitude bins: M_L 1.0 -1.5 (M1), M_L 1.5 - 2.0 (M2) and M_L 2.0 - 2.5 (M3)

302   • Three focal mechanism solutions: FM1 (317°, 59°, -85°), FM2 (292°, 53°, -133°) and FM3

303   (274°, 71°, -128°)

304   Two level of Gaussian noise: 5% and 30%. When D2 is simulated, in order to solve the verse ambiguity

305   of the slip vector, a P-wave polarity is added to the earthquake data to be inverted for the focal

306   mechanism.

307   *Step 3*. For each earthquake simulation the focal mechanism was estimated by inverting the synthetic

308   data with BISTROP (De Matteis et al.; 2016).

309   *Step 4*. In order to analyse the results, we defined five kinds of map to study how the focal mechanism

310   (FM) resolution and error spatially change in the area where ISNet is installed (Table 2):

311

312   • Kagan angle misfit map (KAM)

313   • Map of the focal mechanism parameter misfit (FMM)

- Strike, Dip and Rake error map (FME)

- Kagan angle average map (KAA)

- Kagan angle standard deviation map (KAS)

The Kagan Angle (KA) measures the difference between the orientations of two seismic moment tensors or two double couples. It is the smallest angle needed to rotate the principal axes of one moment tensor to the corresponding principal axes of the other (Kagan et al.; 1991; Tape and Tape; 2012). The smaller the KA between two focal mechanisms, more similar they are. In KAM map, for each node the value of KA between the theoretical and retrieved solution is reported, while in FMM map, the absolute value of the misfit between the strike, dip, and rake angles of the retrieved and theoretical solution is indicated. FME is defined as the error map of strike, dip, and rake in which the uncertainties (standard deviations) are calculated considering all the solutions with probability larger than the 90% (S90) of the maximum probability, corresponding to the best solution retrieved. Additionally, these solutions are used to study how constrained is the FM solution. The KA is calculated between each FM of S90 solutions and the retrieved best solution. The mean and the standard deviation of the resulting KA distribution are plotted in KAA and KAS maps, respectively. The smaller KA mean and std, the more constrained is the obtained fault plane solution (Table 2).

DISCUSSION

We consider the FM1, i.e. the focal mechanism of the1980 Irpinia earthquake located at 10 km depth, first. Looking at Figures 4 and 5, we see the effect of using the three different datasets. Considering D1, we can calculate the FM only for earthquakes with magnitude 2.0-2.5 for which at least 6 polarities are available. As shown by KAM map in Figure 4a, the retrieved solutions are characterized by high KA (> 50°) with limited areas or single nodes with values in the range 40°-50°. Therefore, D1 cannot retrieve with acceptable accuracy the FMs for earthquakes with magnitude 2.0-2.5. The same result is obtained for FM2 and FM3 (Figure 4b-c). Comparing the results of the simulations using D2 and D3

(Figure 5), the accuracy of the retrieved solution is improved when P-wave polarities data are added to spectral level ratios. The areas in KAM map with high value of KA (KA $\geq$ 18°; red or green areas) disappear or are strongly reduced. Nevertheless, even with D2 dataset, the FMs are well retrieved for all magnitudes with the KA misfit mostly lesser than 10°, except in some small areas. The spatial resolution of the network is strongly influenced by the earthquake magnitude. In fact, for both M1 and M2, there are nodes (white areas where we assume the KA = -1 as an indeterminate value) for which the FMs cannot be calculated because less than 6 stations (the minimum number) are available (Table 1). At the same time, the areas better resolved correspond to the region inside the network. With D2 and D3 acceptable solutions are calculated for M1 and M2 earthquakes also outside the network, (Figure 5).

Looking at Figure 6, using the D3 dataset, the dip angle is the best resolved compared with strike and rake angles. For the M2 and M3 focal mechanisms, the misfit of dip is very low (< 8°), followed, in ascending order, by rake and strike that show higher values (10° < misfit < 22°). For M1 (Figure 6a-d-g), rake and strike misfits are larger than 50°, with rake worse resolved than strike. The unresolved areas correspond to the regions outside the seismic network.

The KAA and KAS maps (Figures 7 and 8) show how the network constrains the fault plane solution as a function of the epicentral location. Moreover, Figures 7d-e-f and 8d-e-f indicate that the areas with KA mean and standard deviation greater than 30° and 20°, respectively, are reduced when P-wave polarities and spectral level ratios data are used. On the contrary, only for M1 focal mechanisms, there is no improvement because the number of P-wave polarities is the same for both D2 and D3 datasets (Table 1). The worst constrained regions correspond to a belt surrounding the seismic network, with KA mean < 30° and KA std < 20° for M2 and M3 solutions. For M1, areas with high uncertainty remain outside and inside the network, specifically in the central and eastern sectors.

Looking at the uncertainties of FM parameters, obtained by using the D3 dataset, Figure 9 shows that the dip is the better-constrained parameter with an error < 10°, also for M1 solutions. The rake angle shows an uncertainty lower than 20° for M2 and M3, while it higher than 50° for M1. The strike angle has the highest uncertainty, with values greater than 50° in the eastern and southern sectors of the

map for any analysed magnitudes (M1, M2, and M3). Accuracy improves moving from M1 to M3 earthquakes.

The accuracy of fault plane solutions evaluated using the KA misfit and D3 dataset is similar for FM1, FM2, and FM3, mostly with values lesser than 8° for all the magnitudes (Figure 10). FM2 and FM3 show a slightly higher precision than FM1 in the area inside the seismic network (see FMM, FME, KAA, and KAS maps for FM2 and FM3 in Supplementary Material). In the regions outside the network, where the azimuthal gap increases, the FMs better constrained in descending order are: FM3, FM2, and FM1. This effect should be due to the geometric relationship between the spatial distribution of the seismic stations and the orientation of the principal axes (P, T, B) that characterize the FMs.

Considering the effect of hypocentre depth, the results achieved for earthquakes at 5 km depth, by using the D3 dataset, are overall unchanged (Figure 11). We note that the fault plane solutions are slightly worse resolved due to a smaller number of P-wave polarities available for M2 and M3. The KA misfit generally is lesse than 10°, even though the number and the dimension of areas with misfits> 20° are greater than those obtained considering earthquakes at 10 km depth. Moreover, the dip angle shows a misfit lower than strike and rake angles for M1, M2, and M3; the accuracy of the retrieved FMs parameters is mainly lesse than 8°, as shown in Figure 11.

Previous analyses are carried out considering data affected by 5% Gaussian error. In the last test, we simulated synthetic data adding a 30% Gaussian error. As illustrated in Figure 12, FM solutions show an overall larger misfit, in particular, the KA inside the seismic network is less than 20°. The area best resolved (KA < 8°) is reduced to the central portion of the network. This result indicates that the accuracy of the spectral level ratio estimates is crucial: noisy waveforms with a low signal-to-noise ratio can critically affect the result of the focal mechanism inversion. So, seismic noise as well as the number of available stations, variable due to the operational conditions, strongly influence the capability of the seismic network to retrieve a fault plane solution. Using the results of our simulations, we classified the focal mechanism provided by De Matteis et al. (2016) according to a quality code based on the resolution of fault kinematics (Table 3). In fact, we assigned to focal mechanisms of the Irpinia instrumental seismicity a qualities A, B and C for the solutions that fall into the bins relative to FM3,

394   FM2 and FM1 kinematics, respectively. The quality A, B and C correspond to the average value of KA

395   misfit (FM3=2.4°, FM2=3.1°, FM1=4.5°) calculated for M1, M2 and M3 magnitudes using D3 dataset

396   and considering earthquakes at 10 km depth with 5% Gaussian errors.

397   As last analysis, we carried out a test in a more general framework, without a fixed network

398   configuration. We explored the reliability of focal mechanism estimation as a function of the uniformity

399   of the focal sphere coverage, defined by the number of recording seismic stations and azimuthal gap.

400   We simulated 10400 earthquakes fixing the fault plane solution and varying: 1) the number of seismic

401   stations (6-30), 2) the take-off angle and 3) the azimuth of each single station. For each possible

402   number of seismic stations, we run about 400 simulations, and we randomly sampled the focal sphere

403   varying the azimuth and take-off of the stations, thus changing the geometrical configuration of our

404   virtual network of each simulation. We computed the KA between the theoretical and retrieved focal

405   mechanism (best) solutions using only P-polarities for each simulation. We show the results in Figures

406   13 and S7, as 3-D histograms and 3-D scatter plot, respectively. In Figures 13a, as expected, the

407   number of stations increaseswhile the KA and its range of variation decrease. If the number of stations

408   is less than nine, only few solutions have KA<40°. Figure 13b shows that most value of KA less than

409   30° are obtained for azimuthal gap less than about 80°. In Figure S7, the relation among the KA,

410   azimuthal gap and number of stations is clarified by the three-dimensional spatial point patterns as well

411   by the projections of the data on the three coordinate planes.

412

413   **CONCLUSIONS**

414   We studied the focal mechanism reliability retrieved by the inversion of data recorded by ISNet, a local

415   dense seismic network that monitors the Irpinia Fault System in Southern Italy. Three different datasets

416   of seismological observables are used as input data for focal mechanism determination: a) P-wave

417   polarities, b) P/S long-period spectral amplitude ratios, and c) joint polarities and amplitude ratios.

418   Starting from empirical observations, we computed synthetic data for a regular grid of epicentre

419   locations at two depths (5 and 10 km), for earthquake magnitude in the range 1.0-2.5, and for three

focal mechanism solutions. Two different levels of Gaussian error (5% and 30%) are added to the data.

Our results show that:

- The joint inversion of P-wave polarities and P/S spectral amplitude ratios allows retrieving accurate FM (KA misfit < 8°) also for earthquakes with magnitude ranging between 1.0 and 2.5, at depths of 5 km and 10 km. Due to the low-energy magnitude, the number of P-wave polarities cannot constrain fault plane solutions.

- The spatial resolution analysis of ISNet shows that the most accurate FM solutions are obtained for earthquakes located inside the network with strike, dip and rake misfit < 8°. Nevertheless, outside the network or at its borders, acceptable solutions can be calculated even if the azimuthal coverage is inaadequate (especially for M2 and M3 events). This is due to the geometrical relationship between the seismic stations and the orientation of the principal axes (P, T, B).

- The geometry of the network allows to resolve well fault plane solutions varying between normal and normal-strike focal mechanism with strike, dip and rake misfit generally less than 10° and for the magnitude range 1.5-2.5. The network resolves slightly better normal-strike fault plane solution than pure normal focal mechanism.

- Among the FM parameters, the dip angle shows the lowest uncertainty. Strike and rake angles have higher errors especially for M 1-1.5 earthquakes in the region outside the seismic network.

- Adding a 30% Gaussian error worsens the accuracy of the retrieved FMs. Despite the higher uncertainty fault plane solutions (KA misfit < 20°) are still resolved in the central part of the network, especially for M2 and M3.

The methodology described in this work can be a valid tool to design and test the performance of local seismic networks, aimed at monitoring natural or induced seismicity. Moreover, given a network configuration, it can be used to evaluate the reliability of FMs or to classify fault plane solutions that represent a fundamental information in seismotectonic studies. Although it is a theoretical study, many

446   earthquake scenarios with several magnitude, locations and noise conditions can be simulated to mimic

447   the real seismicity.

448
449
450
451
452
453
454
455
456
457
458
459
460
461
462
463
464
465
466
467
468
469
470
471
472
473
474
475
476
477
478
479
480
481
482
483
484
485
486
487
488
489
490
491
492

REFERENCES

Adinolfi, G. M., Cesca, S., Picozzi, M., Heimann, S., & Zollo, A. (2019). Detection of weak seismic sequences based on arrival time coherence and empiric network detectability: an application at a near fault observatory. *Geophysical Journal International*, *218*(3), 2054-2065.

Adinolfi, G. M., Picozzi, M., Cesca, S., Heimann, S., & Zollo, A. (2020). An application of coherence-based method for earthquake detection and microseismic monitoring (Irpinia fault system, Southern Italy). *Journal of Seismology*, *24*, 979-989.

Amoroso, O., Ascione, A., Mazzoli, S., Virieux, J., & Zollo, A. (2014). Seismic imaging of a fluid storage in the actively extending Apennine mountain belt, southern Italy. *Geophysical Research Letters*, *41*(11), 3802-3809.

Amoruso, A., Crescentini, L., & Scarpa, R. (2005). Faulting geometry for the complex 1980 Campania-Lucania earthquake from levelling data. *Geophysical Journal International*, *162*(1), 156-168.

Bartal, Y., Somer, Z., Leonard, G., Steinberg, D. M., & Horin, Y. B. (2000). Optimal seismic networks in Israel in the context of the Comprehensive Test Ban Treaty. *Bulletin of the seismological society of America*, *90*(1), 151-165.

Bello, S., De Nardis, R., Scarpa, R., Brozzetti, F., Cirillo, D., Ferrarini, F., ... & Lavecchia, G. (2021). Fault Pattern and Seismotectonic Style of the Campania–Lucania 1980 Earthquake (M w 6.9, Southern Italy): New Multidisciplinary Constraints. Front. *Earth Sci*, *8*, 608063.

Ben-Menahem, A., and S. J. Singh (1981). Seismic Waves and Sources, 1108 p, Springer-Verlag, New York.

Bentz, Stephan, P. Martínez-Garzón, G. Kwiatek, M. Bohnhoff, and J. Renner (2018). Sensitivity of Full Moment Tensors to Data Preprocessing and Inversion Parameters: A Case Study from the Salton Sea Geothermal Field. Bull. Seismol. Soc. Am. 108, 588–603, doi 10.1785/0120170203

Bernard, P., & Zollo, A. (1989). The Irpinia (Italy) 1980 earthquake: detailed analysis of a complex normal faulting. *Journal of Geophysical Research: Solid Earth*, *94*(B2), 1631-1647.

Boatwright, J. (1980). A spectral theory for circular seismic sources; simple estimates of source dimension, dynamic stress drop, and radiated seismic energy, *Bull. Seismol. Soc. Am.*, **70** (7), 1–27.

Brillinger, D. R., A. Udías, and B. A. Bolt (1980). A probability model for regional focal mechanism solutions, *Bull. Seism. Soc. Am.* **70**, 149- 170.

Cesca, S., Heimann, S., Stammler, K., & Dahm, T. (2010). Automated procedure for point and kinematic source inversion at regional distances. *Journal of Geophysical Research: Solid Earth*, *115*(B6).

Cocco, M., Chiarabba, C., Di Bona, M., Selvaggi, G., Margheriti, L., Frepoli, A., ... & Campillo, M. (1999). The April 1996 Irpinia seismic sequence: evidence for fault interaction. *Journal of Seismology*, *3*(1), 105-117.

Delouis, B. (2014). FMNEAR: Determination of focal mechanism and first estimate of rupture directivity using near-source records and a linear distribution of point sources. *Bulletin of the Seismological Society of America*, *104*(3), 1479-1500.

De Matteis, R., Matrullo, E., Rivera, L., Stabile, T. A., Pasquale, G., & Zollo, A. (2012). Fault delineation and regional stress direction from the analysis of background microseismicity in the southern Apennines, Italy. *Bulletin of the Seismological Society of America*, *102*(4), 1899-1907.

De Matteis, R., Convertito, V., & Zollo, A. (2016). BISTROP: Bayesian inversion of spectral-level ratios and P-wave polarities for focal mechanism determination. *Seismological Research Letters*, *87*(4), 944-954.

Dreger, D. S., Lee, W. H. K., Kanamori, H., Jennings, P. C., & Kisslinger, C. (2003). Time-domain moment tensor INVerse codel (TDMT-INVC) release 1.1. *International Handbook of Earthquake and Engineering Seismology, WHK Lee, H. Kanamori, PC Jennings, and C. Kisslinger (Editors), Vol. B*, 1627.

Festa, G., Adinolfi, G. M., Caruso, A., Colombelli, S., De Landro, G., Elia, L., ... & Zollo, A. (2021). Insights into Mechanical Properties of the 1980 Irpinia Fault System from the Analysis of a Seismic Sequence. *Geosciences*, *11*(1), 28.

Hardebeck, J., and M. Shearer (2003). Using S/P Amplitude Ratios to Constrain the Focal Mechanisms of Small Earthquakes, *Bull. Seism. Soc. Am.* **93**, 6, pp. 2434–2444, December 2003.

Hardt, M., & Scherbaum, F. (1994). The design of optimum networks for aftershock recordings. *Geophysical Journal International*, *117*(3), 716-726.

Havskov, J., Ottemöller, L., Trnkoczy, A., Bormann, P. (2012): Seismic Networks. - In: Bormann, P. (Ed.), *New Manual of Seismological Observatory Practice 2 (NMSOP-2)*, Potsdam : Deutsches GeoForschungsZentrum GFZ, 1-65.

Julian, B. R., and G. R. Foulger (1996). Earthquake mechanisms from linear-programming inversion of seismic-wave amplitude ratios, *Bull. Seism. Soc. Am.* **86** (4), 972-980.

Kagan, Y. Y. (1991). 3-D rotation of double-couple earthquake sources. *Geophysical Journal International*, *106*(3), 709-716.

Kisslinger, C., J. R. Bowman, and K. Koch (1981). Procedures for computing focal mechanisms from local (SV/P) z data, *Bull. Seism. Soc. Am.* **71** (6), 1719-1729.

Kwiatek, G., P. Martínez-Garzón, and M. Bohnhoff (2016). HybridMT: A MATLAB Software Package for Seismic Moment Tensor Inversion and Refinement. Seismol. Res. Lett.

Kwiatek, G. and Y. Ben-Zion (2016). Theoretical limits on detection and analysis of small earthquakes. Journal of Geophysical Research-Solid Earth 121, doi 10.1002/2016JB012908

Kwiatek, G. and Y. Ben-Zion (2020). Detection Limits and Near-Field Ground Motions of Fast and Slow Earthquakes. Journal of Geophysical Research: Solid Earth 125, e2019JB018935, doi 10.1029/2019JB018935

Matrullo E., R. De Matteis, C. Satriano, O. Amoroso, and A. Zollo (2013). An improved 1D seismic velocity model for seismological studies in the Campania-Lucania region (Southern Italy), *Geophys. J. Int.* **195**, Issue 1, pp.460-473, doi: 10.1093/gji/ggt224.

Michele, M., S. Custódio, and A. Emolo (2014). Moment tensor resolution: case study of the Irpinia Seismic Network, Southern Italy, *Bull. Seismol. Soc. Am.* **104**, 1348-1357, doi: 10.1785/0120130177.

Pantosti, D., & Valensise, G. (1990). Faulting mechanism and complexity of the November 23, 1980, Campania-Lucania earthquake, inferred from surface observations. *Journal of Geophysical Research: Solid Earth*, *95*(B10), 15319-15341.

Pasquale, G., De Matteis, R., Romeo, A., & Maresca, R. (2009). Earthquake focal mechanisms and stress inversion in the Irpinia Region (southern Italy). *Journal of seismology*, *13*(1), 107-124.

Reasenberg, P., & Oppenheimer, D. USGS (1985). FPFIT, FPPLOT, and FPPAGE: Fortran computer programs for calculating and displaying earthquake fault-plane solutions. *US Geol. Surv. Open-File Rept. 85, 739*.

Satriano, C., Elia, L., Martino, C., Lancieri, M., Zollo, A., & Iannaccone, G. (2011). PRESTo, the earthquake early warning system for southern Italy: Concepts, capabilities and future perspectives. *Soil Dynamics and Earthquake Engineering*, *31*(2), 137-153.

Snoke, J. A., Lee, W. H. K., Kanamori, H., Jennings, P. C., & Kisslinger, C. (2003). FOCMEC: Focal mechanism determinations. *International handbook of earthquake and engineering seismology*, *85*, 1629-1630.

Stabile, T. A., Satriano, C., Orefice, A., Festa, G., & Zollo, A. (2012). Anatomy of a microearthquake sequence on an active normal fault. *Scientific reports*, *2*(1), 1-7.

Steinberg, D. M., Rabinowitz, N., Shimshoni, Y., & Mizrachi, D. (1995). Configuring a seismographic network for optimal monitoring of fault lines and multiple sources. *Bulletin of the seismological society of America*, *85*(6), 1847-1857.

Sokos, E., & Zahradník, J. (2013). Evaluating centroid-moment-tensor uncertainty in the new version of ISOLA software. *Seismological Research Letters*, *84*(4), 656-665.

Tape, W., & Tape, C. (2012). A geometric setting for moment tensors. *Geophysical Journal International*, *190*(1), 476-498.

Tarantino, S., Colombelli, S., Emolo, A., & Zollo, A. (2019). Quick determination of the earthquake focal mechanism from the azimuthal variation of the initial P-wave amplitude. *Seismological Research Letters*, *90*(4), 1642-1649.

Trnkoczy, A., Bormann, P., Hanka, W., Holcomb, L. G., & Nigbor, R. L. (2009). Site selection, preparation and installation of seismic stations. In *New Manual of Seismological Observatory Practice (NMSOP)* (pp. 1-108). Deutsches GeoForschungsZentrum GFZ.

Vavrycuk, V., P. Adamova, J. Doubravová, and H. Jakoubková (2017). Moment Tensor Inversion Based on the Principal Component Analysis of Waveforms: Method and Application to Microearthquakes in West Bohemia, Czech Republic. Seismological Research Letters 88, 1303–1315, doi 10.1785/0220170027

Weber, E., Iannaccone, G., Zollo, A., Bobbio, A., Cantore, L., Corciulo, M., ... & Satriano, C. (2007). Development and testing of an advanced monitoring infrastructure (ISNet) for seismic early-warning applications in the Campania region of southern Italy. In *Earthquake early warning systems* (pp. 325-341). Springer, Berlin, Heidelberg.

Zollo, A., & Bernard, P. (1991). Fault mechanisms from near-source data: joint inversion of S polarizations and P polarities. *Geophysical Journal International*, *104*(3), 441-451.

TABLES

Depth 5 km	Max Distance (km)	No. P-polarities
M_L 1.0 -1.5	30	1
M_L 1.5 - 2.0	49	1
M_L 2.0 - 2.5	57	4
Depth 10 km	Max Distance (km)	No. P-polarities
M_L 1.0 -1.5	33	1
M_L 1.5 - 2.0	40	5
M_L 2.0 - 2.5	66	6

Table 1 Maximum distance of the farthest triggered seismic station and number of P-wave polarities as function of earthquake magnitude and depth. The values, empirically derived from the ISNet bulletin, are used for the earthquake simulations.

Figure No.	Map	Focal Mechanism Solution	Magnitude Bin	Depth	Noise Level	Dataset
4	Kagan angle misfit	FM1, FM2, FM3	M3	10 km	5%	D1
5	Kagan angle misfit	FM1	M1, M2, M3	10 km	5%	D2, D3
6	focal mechanism parameter misfit	FM1	M1, M2, M3	10 km	5%	D3
7	Kagan angle average	FM1	M1, M2, M3	10 km	5%	D2, D3
8	Kagan angle standard deviation	FM1	M1, M2, M3	10 km	5%	D2, D3
9	focal mechanism error	FM1	M1, M2, M3	10 km	5%	D3
10	Kagan angle misfit	FM1, FM2, FM3	M1, M2, M3	10 km	5%	D3
11	focal mechanism parameter misfit	FM1	M1, M2, M3	5 km	5%	D3
12	Kagan angle misfit	FM1	M1, M2, M3	10 km	30%	D3

Table 2. Summary of the Figures 4-12 with parameters used for earthquake simulations whose results are represented as a specific map.

P-plunge (°)	P-trend (°)	T-plunge (°)	T-trend (°)	Strike (°)	Dip (°)	Rake (°)	Quality
55	344	31	196	325	20	-40	A
51	334	36	181	320	15	-30	A
55	14	31	226	355	20	-40	A
53	205	34	49	180	15	-40	A
55	72	33	272	35	15	-50	A
51	177	32	37	290	80	-110	A
54	292	34	91	10	80	-80	A
77	146	9	7	270	55	-100	B
80	235	10	55	325	55	-90	B
76	103	2	6	110	45	-70	B
76	117	2	214	290	45	-110	B
76	82	7	199	275	40	-110	B
75	190	15	10	280	60	-90	B
75	205	15	25	295	60	-90	B
85	230	5	50	140	40	-90	B
83	146	0	53	150	45	-80	B
80	240	10	60	330	55	-90	B
81	233	5	353	270	50	-80	B
81	347	5	227	130	50	-100	B
55	93	10	198	255	45	-140	C
55	133	10	238	295	45	-140	C
48	130	2	38	275	60	-140	C
48	305	2	37	340	60	-40	C
55	202	7	102	345	60	-130	C
58	121	2	27	270	55	-130	C
58	131	2	37	280	55	-130	C
55	342	7	242	125	60	-130	C
47	138	11	36	165	50	-30	C
49	182	14	289	340	45	-150	C
58	151	2	57	300	55	-130	C
49	168	14	61	190	45	-30	C
59	308	15	64	355	65	-60	C
57	306	14	59	115	40	-140	C
57	76	14	189	245	40	-140	C
45	85	6	348	225	65	-140	C
55	22	7	282	165	60	-130	C
57	241	14	354	50	40	-140	C
55	98	7	198	135	60	-50	C
51	115	2	22	145	55	-40	C
55	147	7	47	290	60	-130	C

722

Table 3. Fault plane solutions of instrumental seismicity occurred in Irpinia region in 2005-2008 and calculated by De Matteis et al., (2012). The solutions are classified according to a quality code based on the resolution of fault plane kinematics as derived in this study. The result of our simulations suggests a quality as follows: FM1=C, FM2=B, FM3=A.

727
728
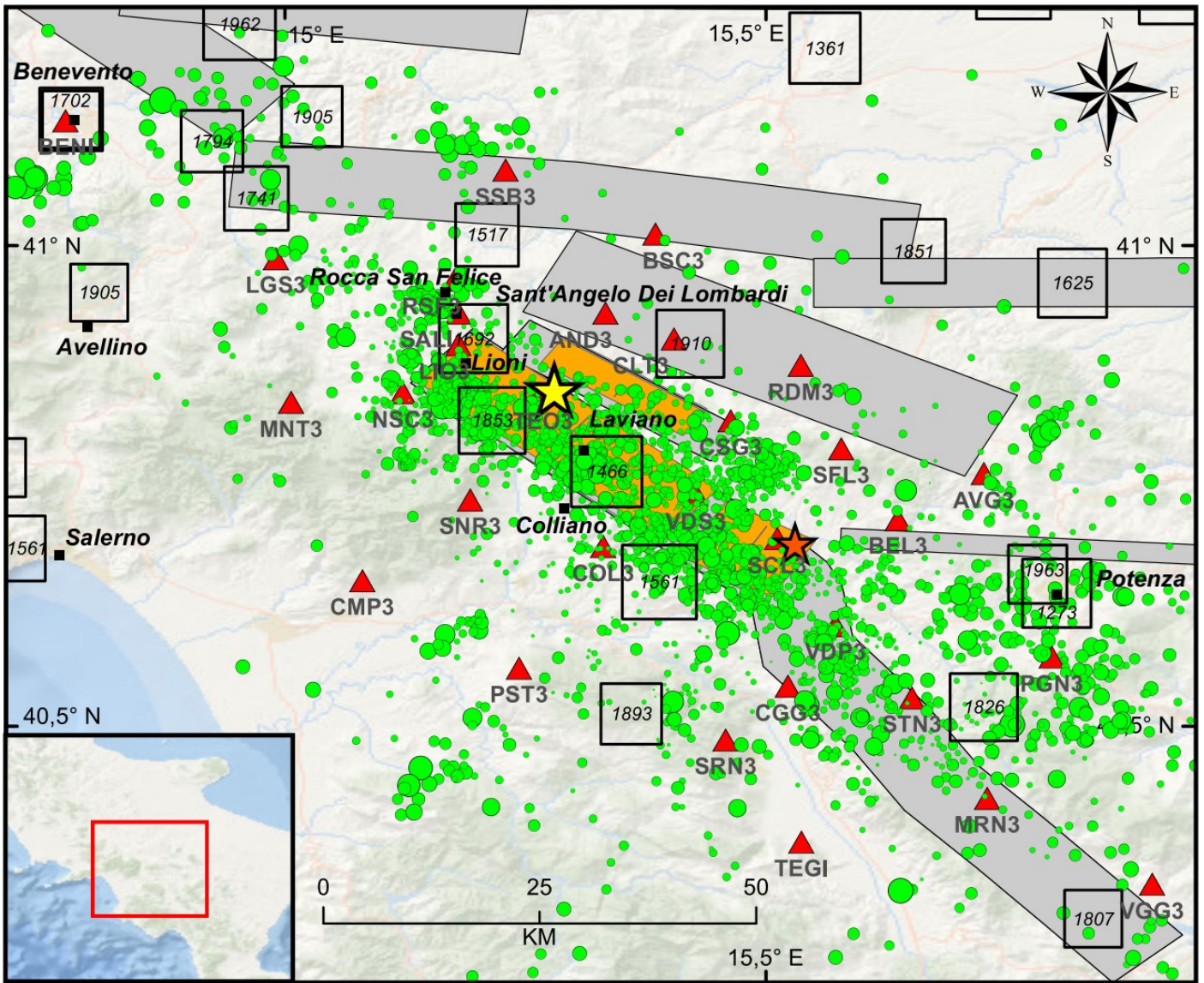
FIGURES

Figure 1. Epicentral map of the earthquakes (green circles) recorded by Irpinia Seismic Network (ISNet, red triangles) from 2008 to 2020 (http://isnet-bulletin.fisica.unina.it/cgi-bin/isnet-events/isnet.cgi). The yellow and orange stars refer to the epicentral location of the 1980, M 6.9, and of the 1996, M 4.9 earthquakes, respectively. Historical seismicity is shown with black squares (I0 ≥ 6–7 MCS). Seismogenic sources related to the Irpinia fault system are indicated by orange rectangles; potential sources for earthquakes larger than M 5.5 in surrounding areas are indicated in grey (Database of Individual Seismogenic Sources, DISS, Version 3.2.1)
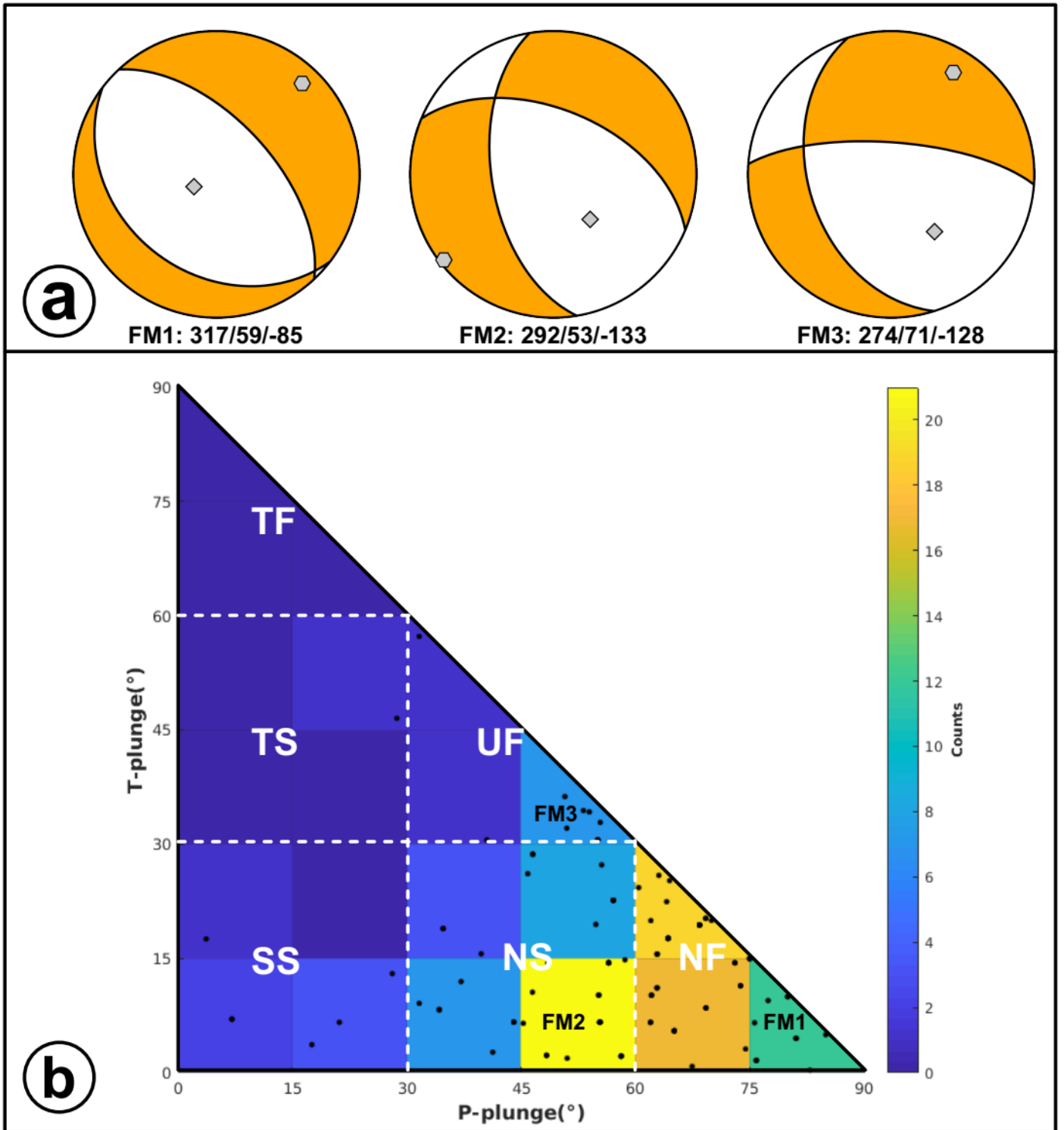
Figure 2. Fault plane solutions used for earthquake simulations. a) From left to right: 1) Ms 6.9, 23rd November 1980 (FM1; Westaway) 2) and 3) Median focal mechanism found from solutions of the 1st (FM2) and 5th (FM3) most populated bin of histogram of panel b. b) Fault plane solutions (black dots) are classified according to the plunge of P- and T-axes with the specific tectonic regimes (Legend: NF, normal fault; NS, normal-strike; SS, strike-slip; TF, thrust ; TS, thrust-strike; UF, unknown fault). The number of earthquakes (colour bar) is counted in bins of 15° × 15°.
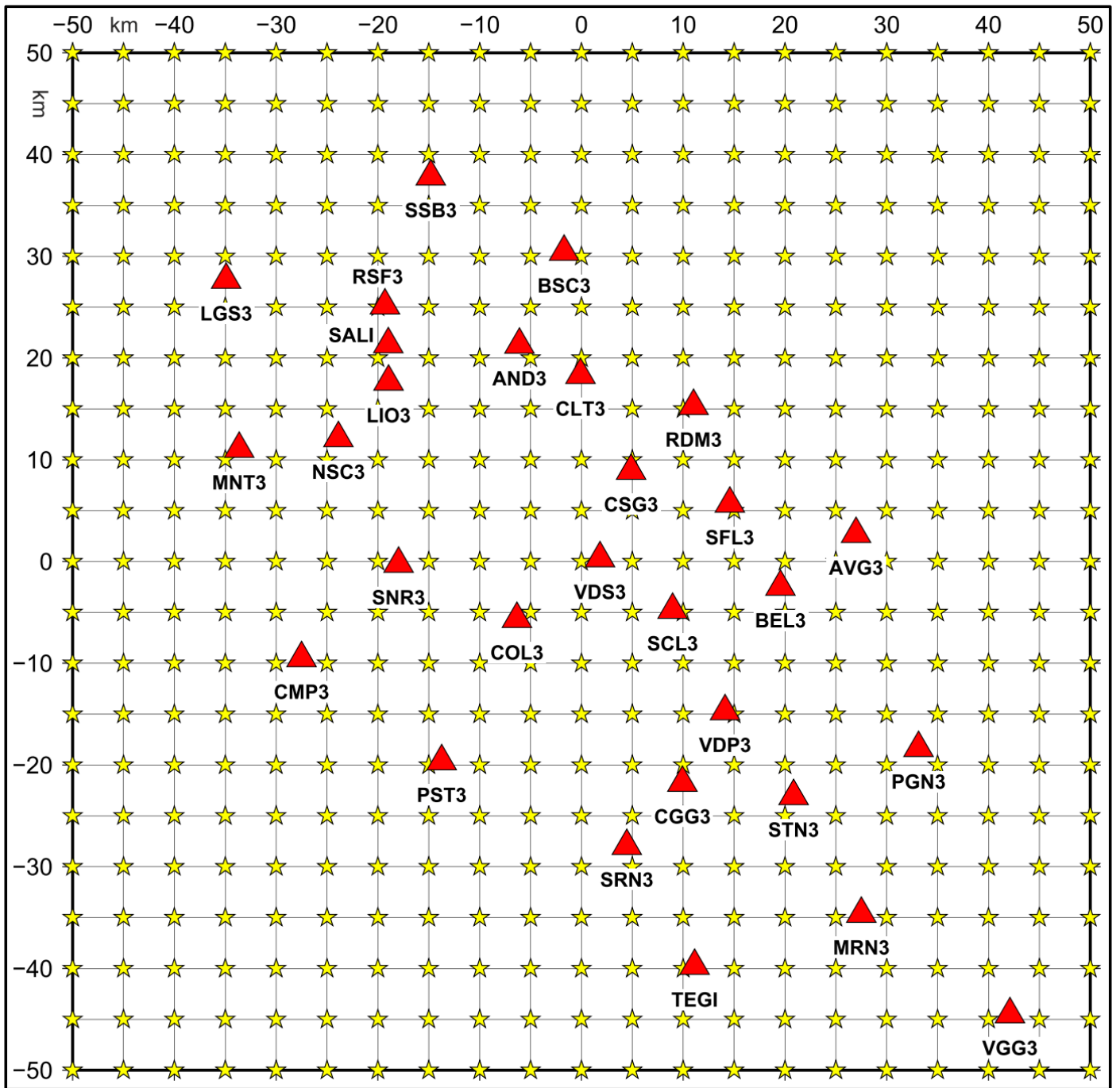
Figure 3. Regular grid of epicentres (yellow stars) used for simulating earthquakes. The area is 100x100 km^2 with 5 km of spacing along both horizontal coordinates. Irpinia Seismic Network (ISNet) is reported with red triangles.
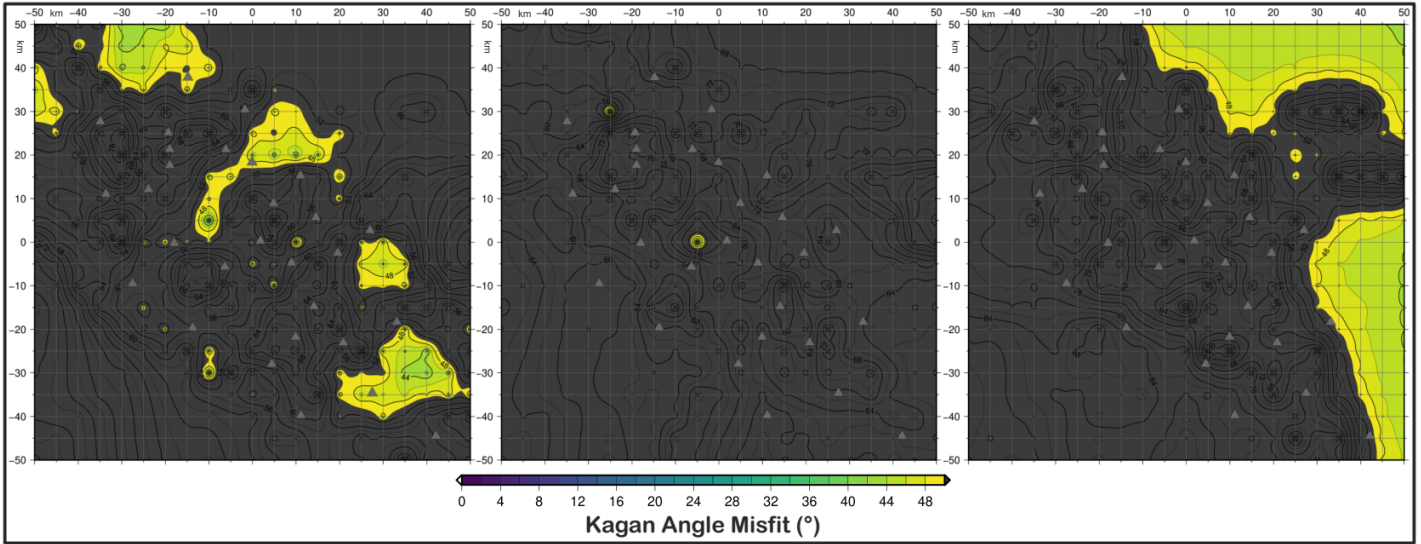
Figure 4. KAM (Kagan angle misfit) map for retrieved focal mechanisms with D1 dataset as input data and simulating earthquakes with M3 magnitude and FM1 (a), FM2 (b) and FM3 (c) theoretical fault plane solution at 10 km depth.
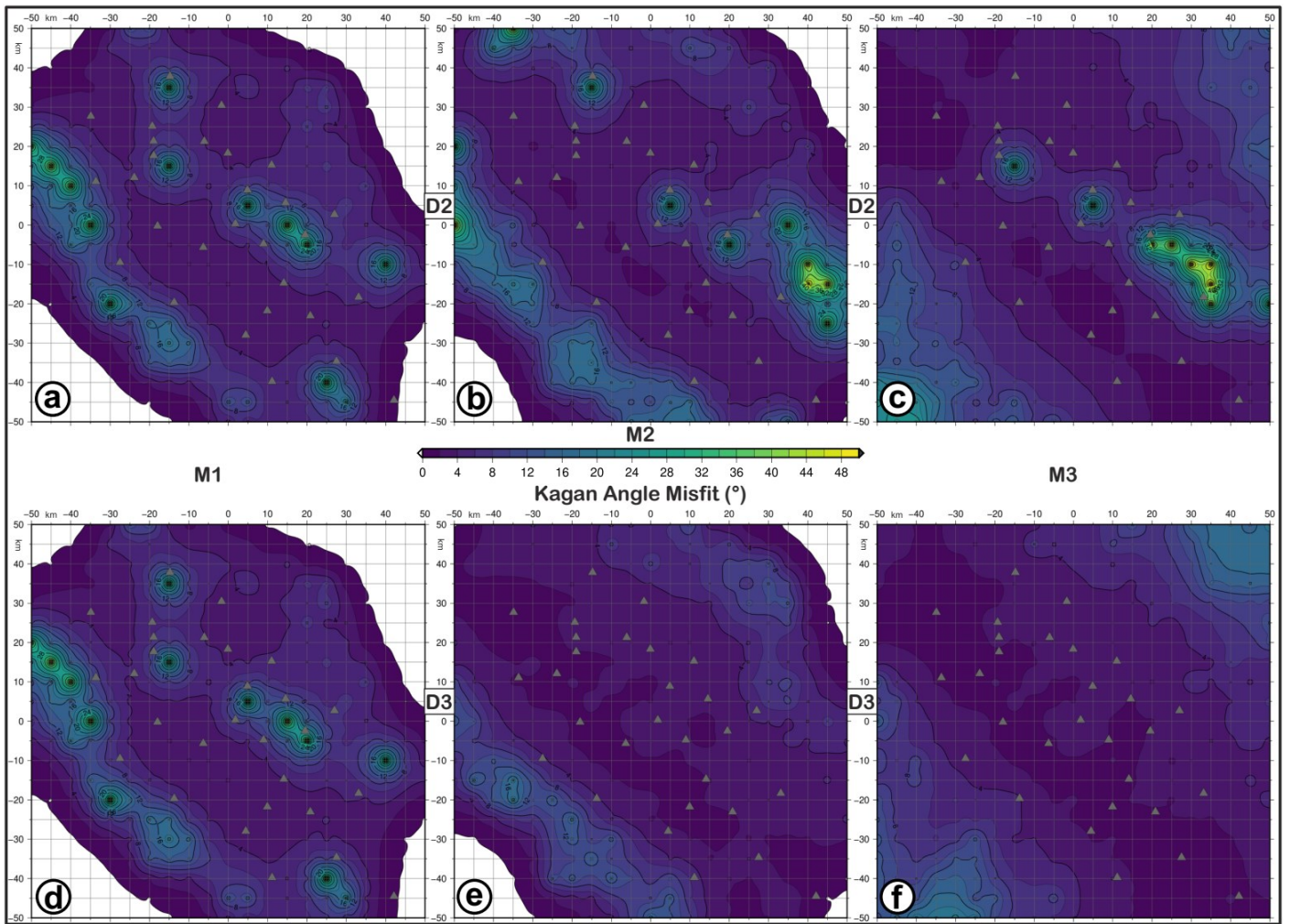
Figure 5. KAM (Kagan angle misfit) map for retrieved focal mechanisms with D2 (a, b, c) and D3 (d, e, f) datasets as input data and simulating earthquakes with M1 (a, d), M2 (b, e) and M3 (c, f) magnitudes and FM1 theoretical fault plane solution at 10 km depth. The level of Gaussian noise is set to 5%.
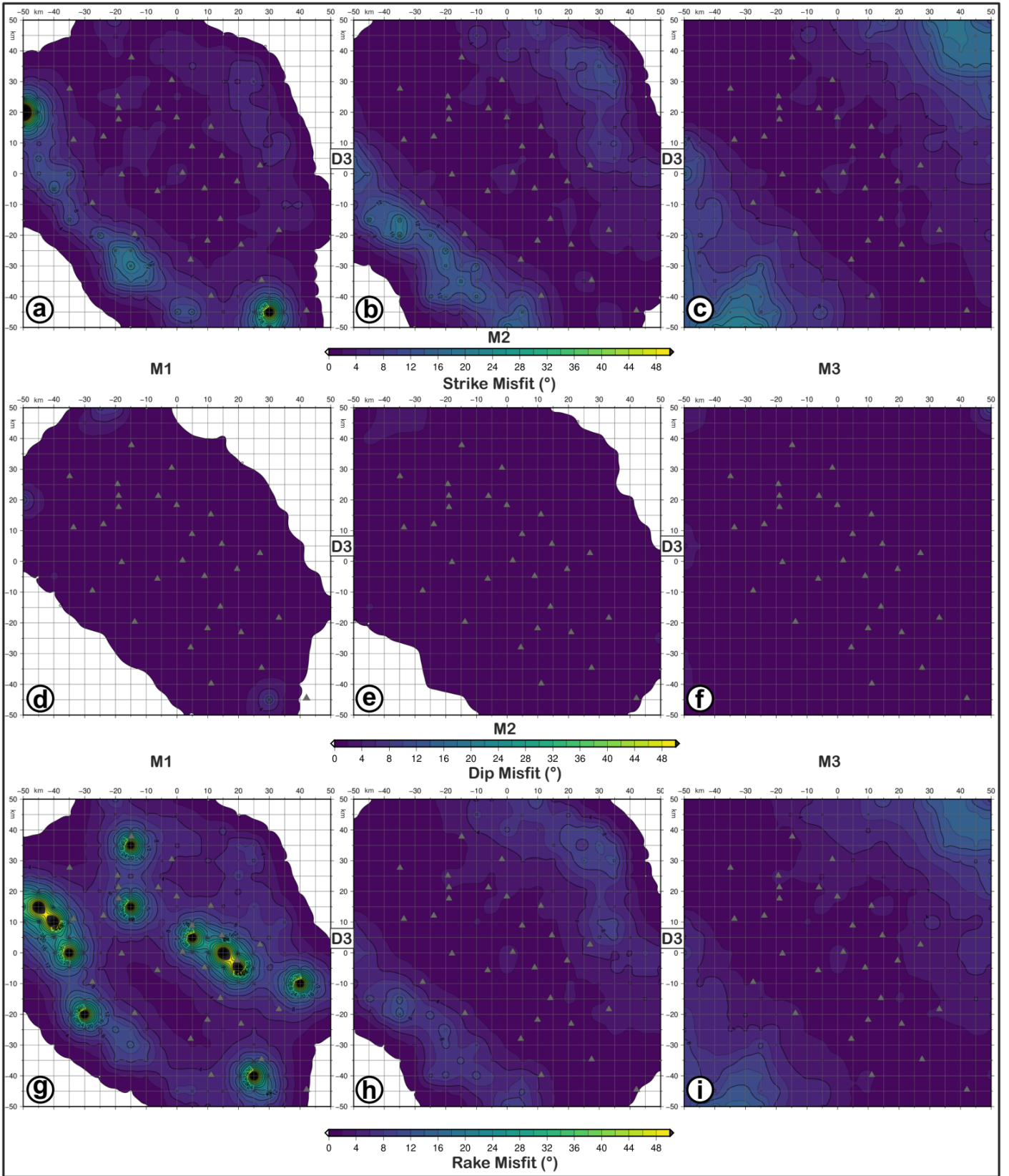
Figure 6. FMM (focal mechanism parameter misfit) maps for retrieved focal mechanisms with D3 datasets as input data and simulating earthquakes with M1 (a, d, g), M2 (b, e, h) and M3 (c, f, i) magnitudes and FM1 theoretical fault plane solution at 10 km depth. a, b, c refer to strike misfit; d, e, f refer to dip misfit; g, h, i refer to rake. The level of Gaussian noise is set to 5%.
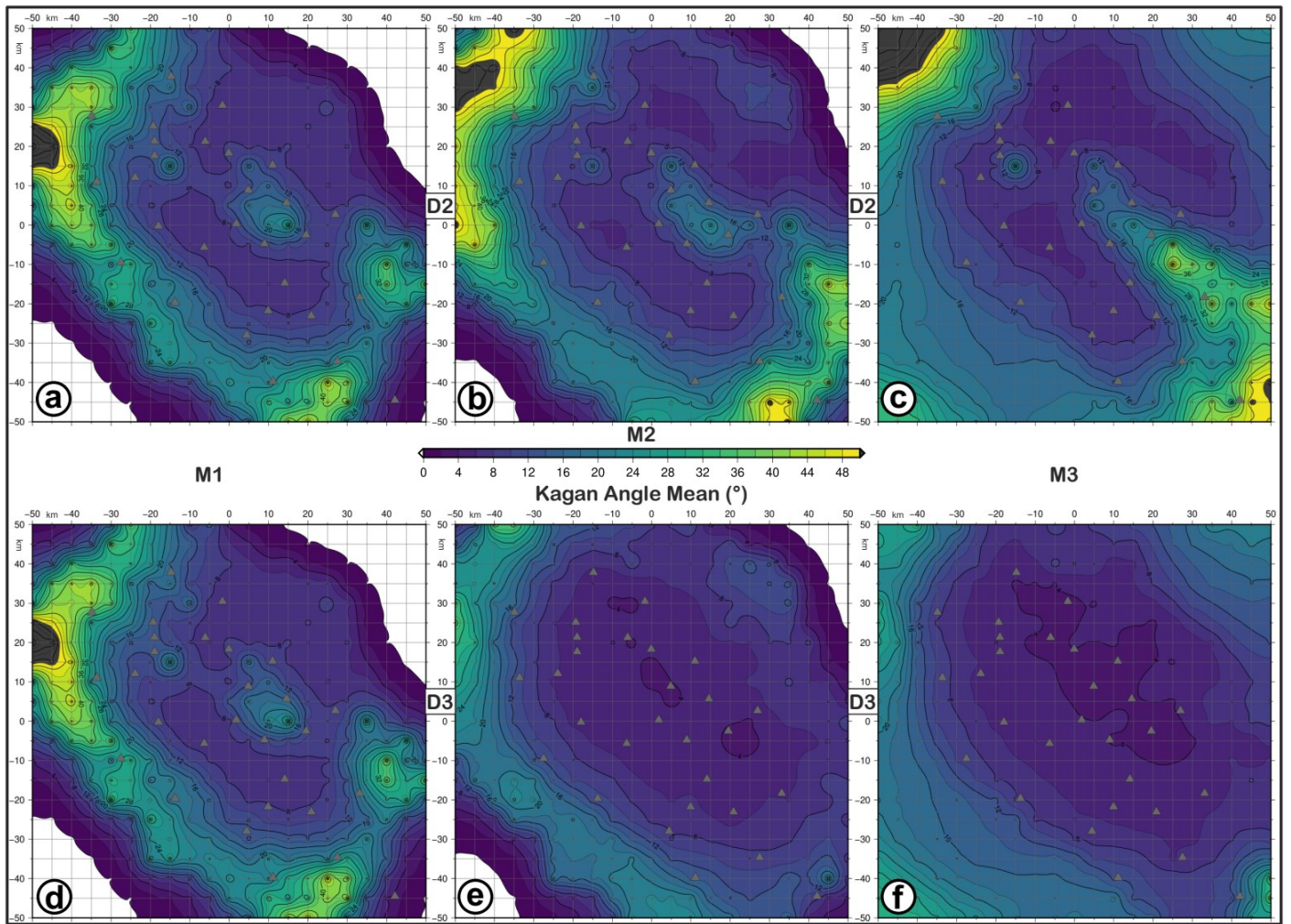
Figure 7. KAA (Kagan angle average) maps for retrieved focal mechanisms with D2 (a, b, c) and D3 (d, e, f) datasets as input data and simulating earthquakes with M1 (a, d), M2 (b, e) and M3 (c, f) magnitudes and FM1 theoretical fault plane solution at 10 km depth. The level of Gaussian noise is set to 5%.

820
821
822
823
824
825
826
827
828
829
830
831
832
833
834
835
836
837
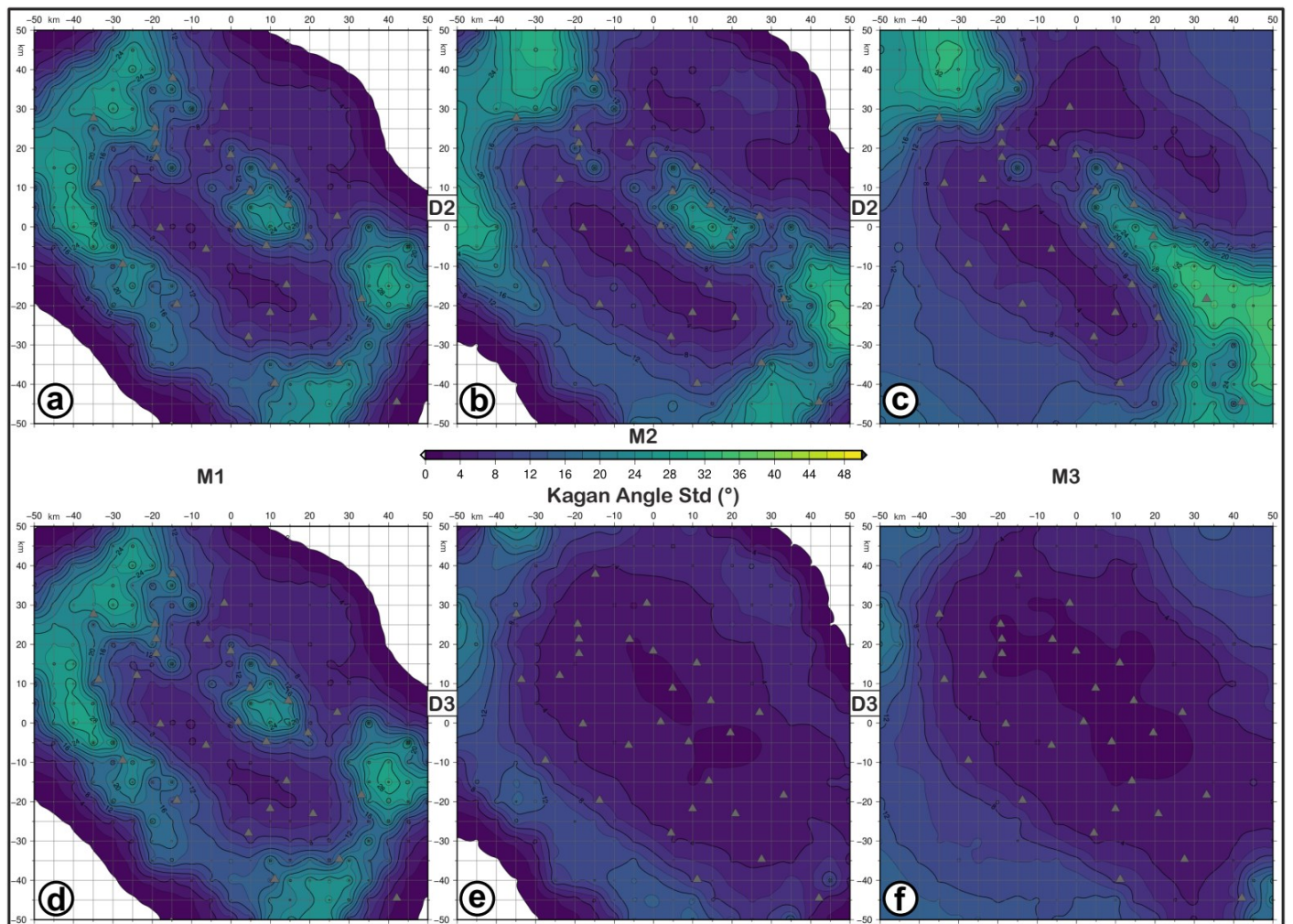
Figure 8. KAS (Kagan angle standard deviation) maps for retrieved focal mechanisms with D2 (a, b, c) and D3 (d, e, f) datasets as input data and simulating earthquakes with M1 (a, d), M2 (b, e) and M3 (c, f) magnitudes and FM1 theoretical fault plane solution at 10 km depth. The level of Gaussian noise is set to 5%.
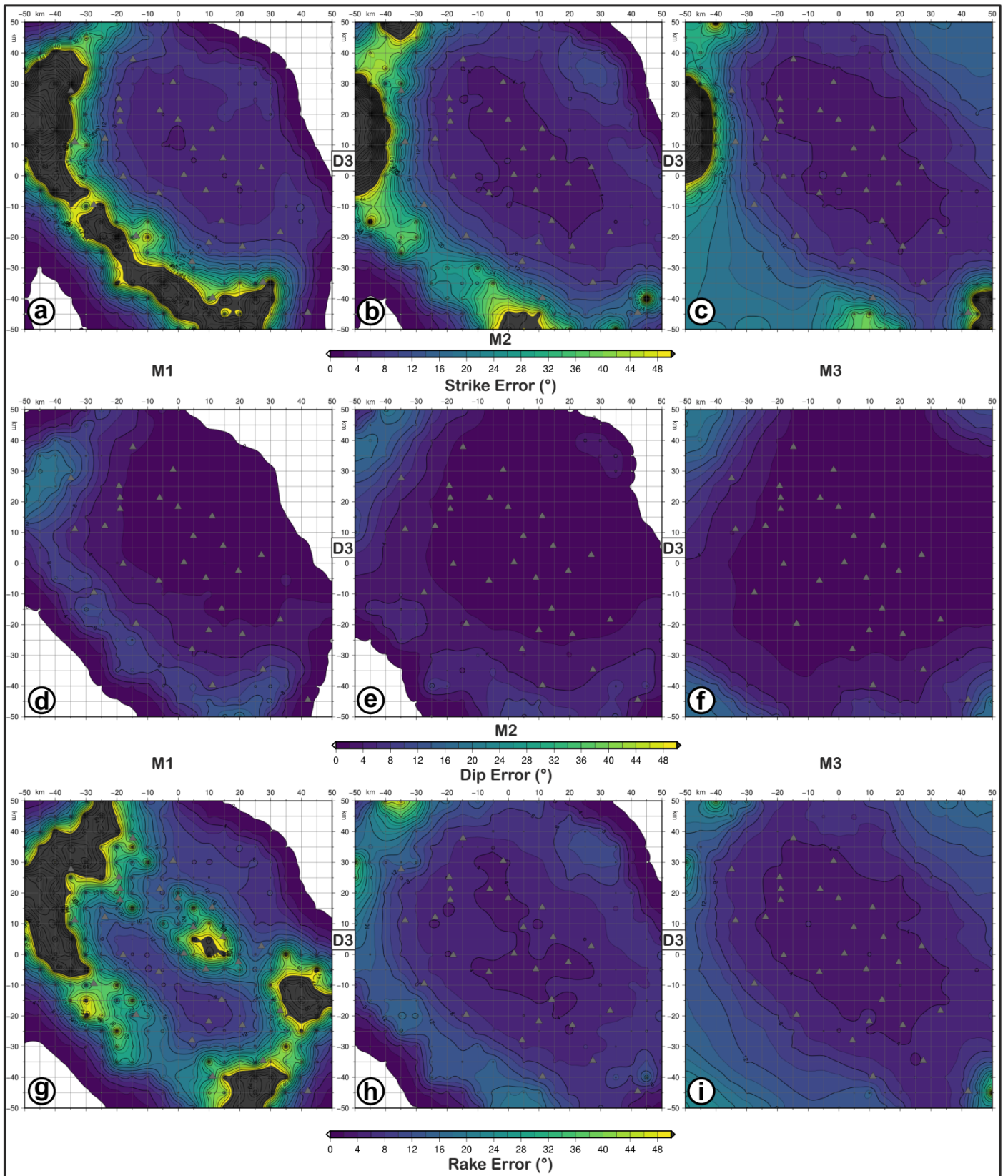
Figure 9. FME (strike, dip and rake error) maps for retrieved focal mechanisms with D3 datasets as input data and simulating earthquakes with M1 (a, d, g), M2 (b, e, h) and M3 (c, f, i) magnitudes and FM1 theoretical fault plane solution at 10 km depth. a, b, c refer to strike error; d, e, f refer to dip error; g, h, i refer to rake error. The level of Gaussian noise is set to 5%.
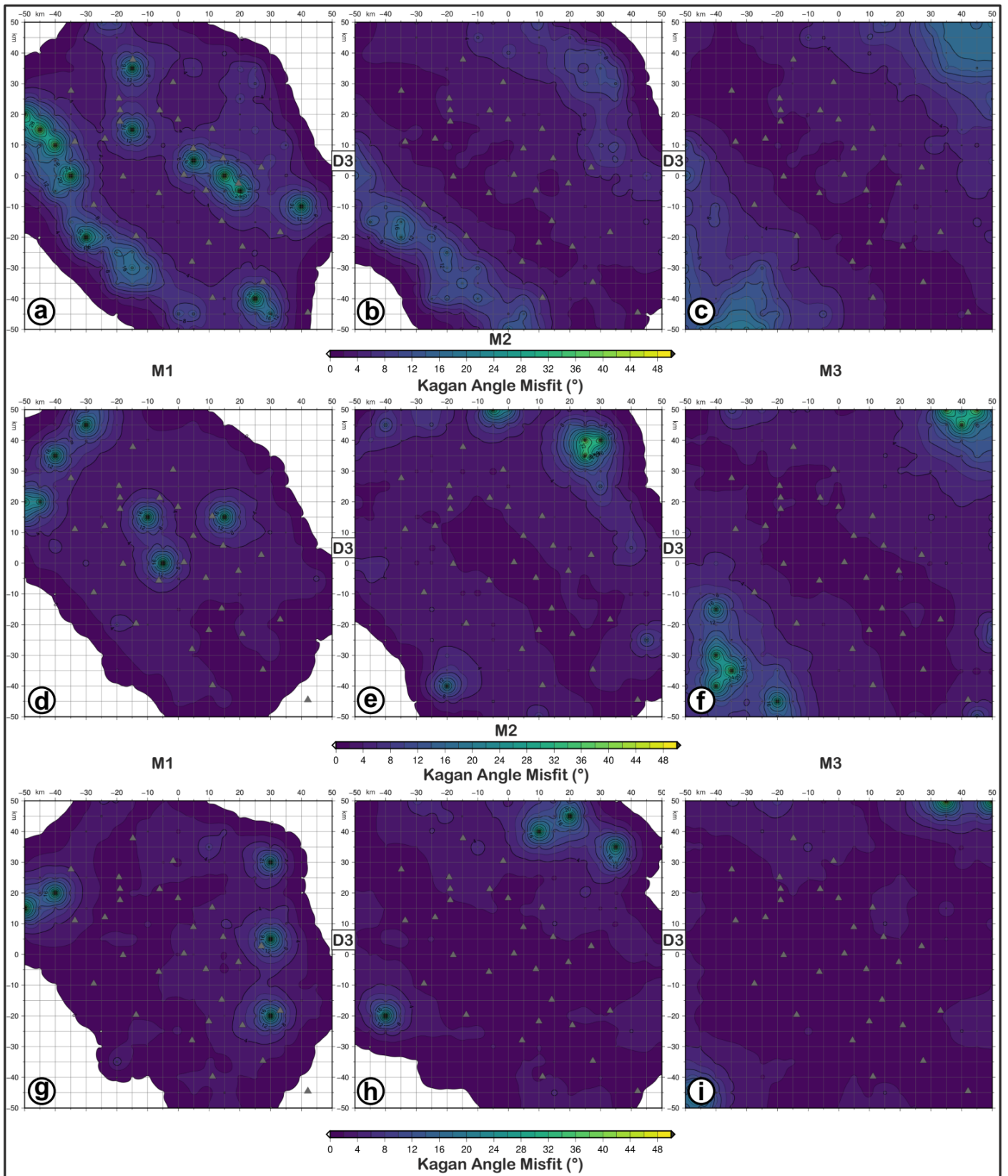
Figure 10. KAM (Kagan angle misfit) maps for retrieved focal mechanisms with D3 datasets as input data and simulating earthquakes with M1 (a, d, g), M2 (b, e, h) and M3 (c, f, i) magnitudes and FM1 (a, b, c), FM2 (d, e, f) and   FM3 (g, h, i) theoretical fault plane solution at 10 km depth. The level of Gaussian noise is set to 5%.
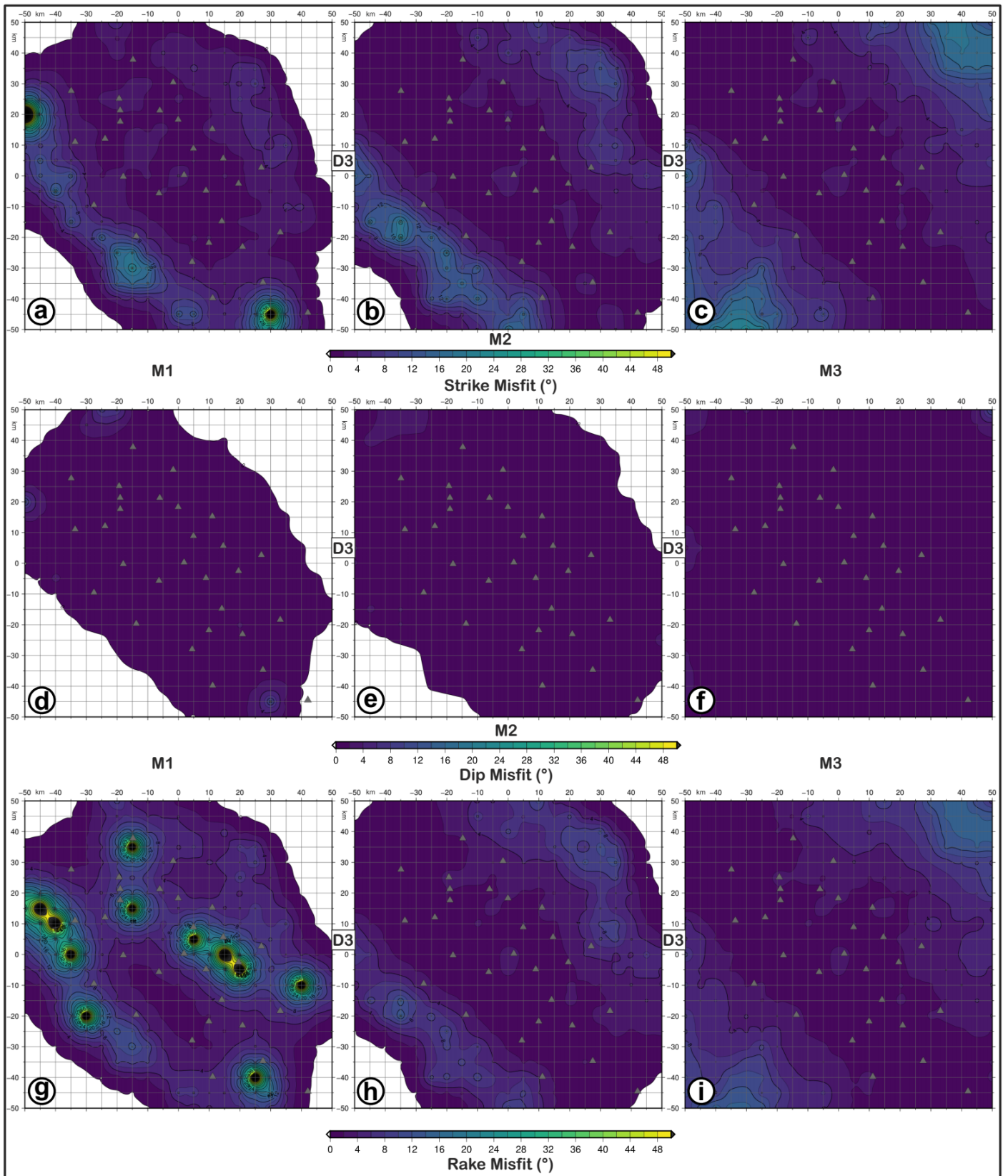
Figure 11. FMM (focal mechanism parameter misfit) maps for retrieved focal mechanisms with D3 datasets as input data and simulating earthquakes with M1 (a, d, g), M2 (b, e, h) and M3 (c, f, i) magnitudes and FM1 theoretical fault plane solution at 5 km depth. a, b, c refer to strike misfit; d, e, f refer to dip misfit; g, h, i refer to rake. The level of Gaussian noise is set to 5%.
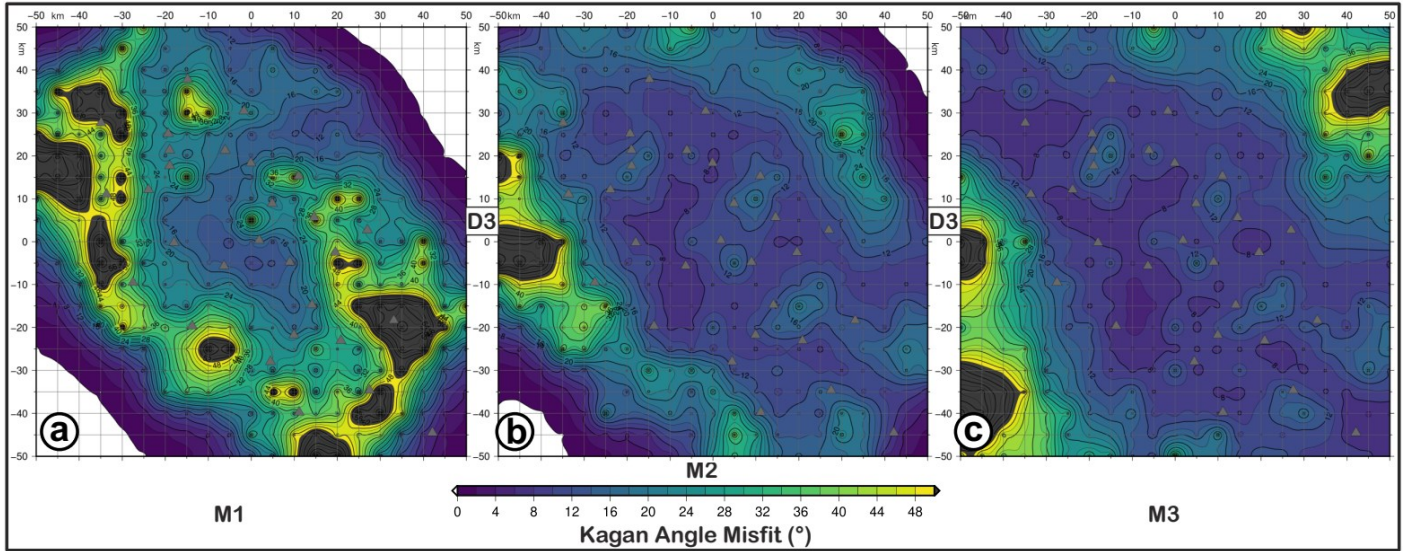
Figure 12. KAM (Kagan angle misfit) map for retrieved focal mechanisms with D3 (a, b, c) datasets as input data and simulating earthquakes with M1 (a), M2 (b) and M3 (c) magnitudes and FM1 theoretical fault plane solution at 10 km depth. The level of Gaussian noise is set to 30%.
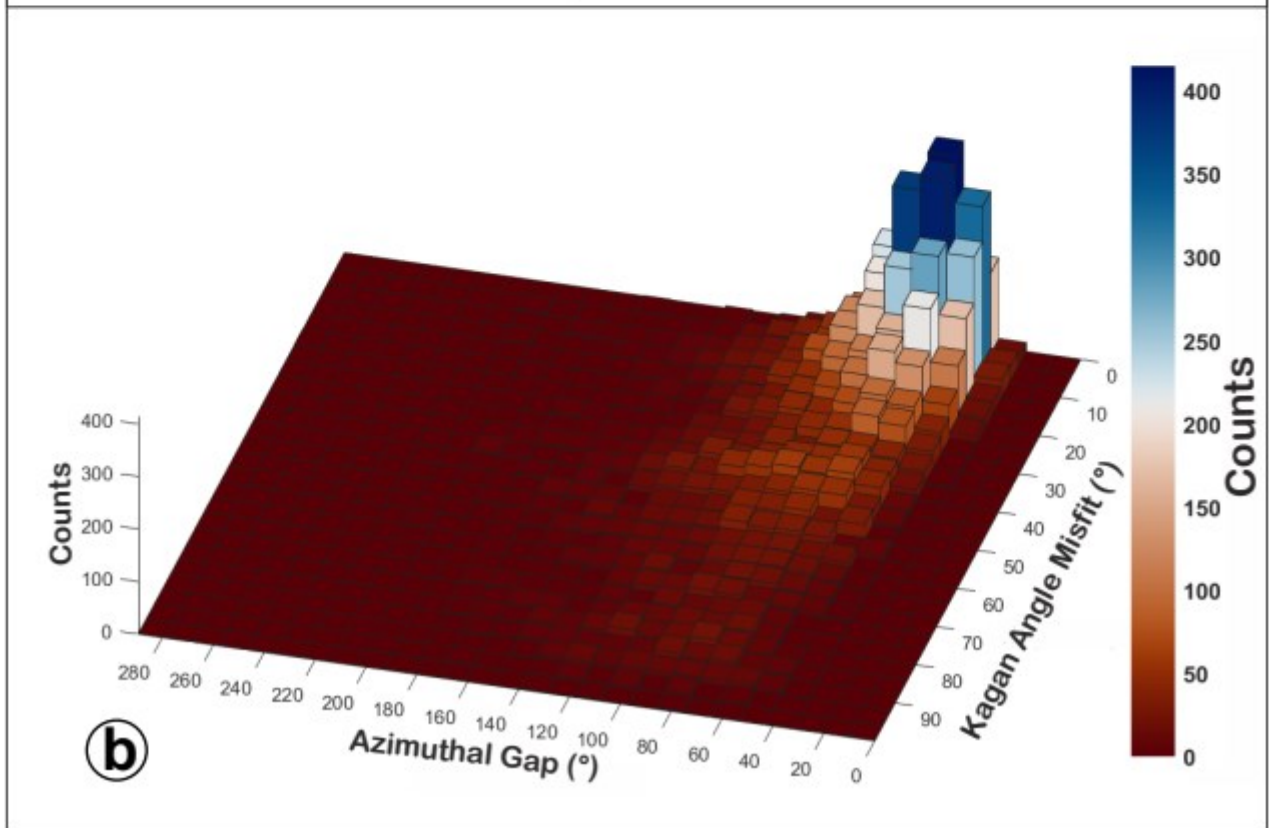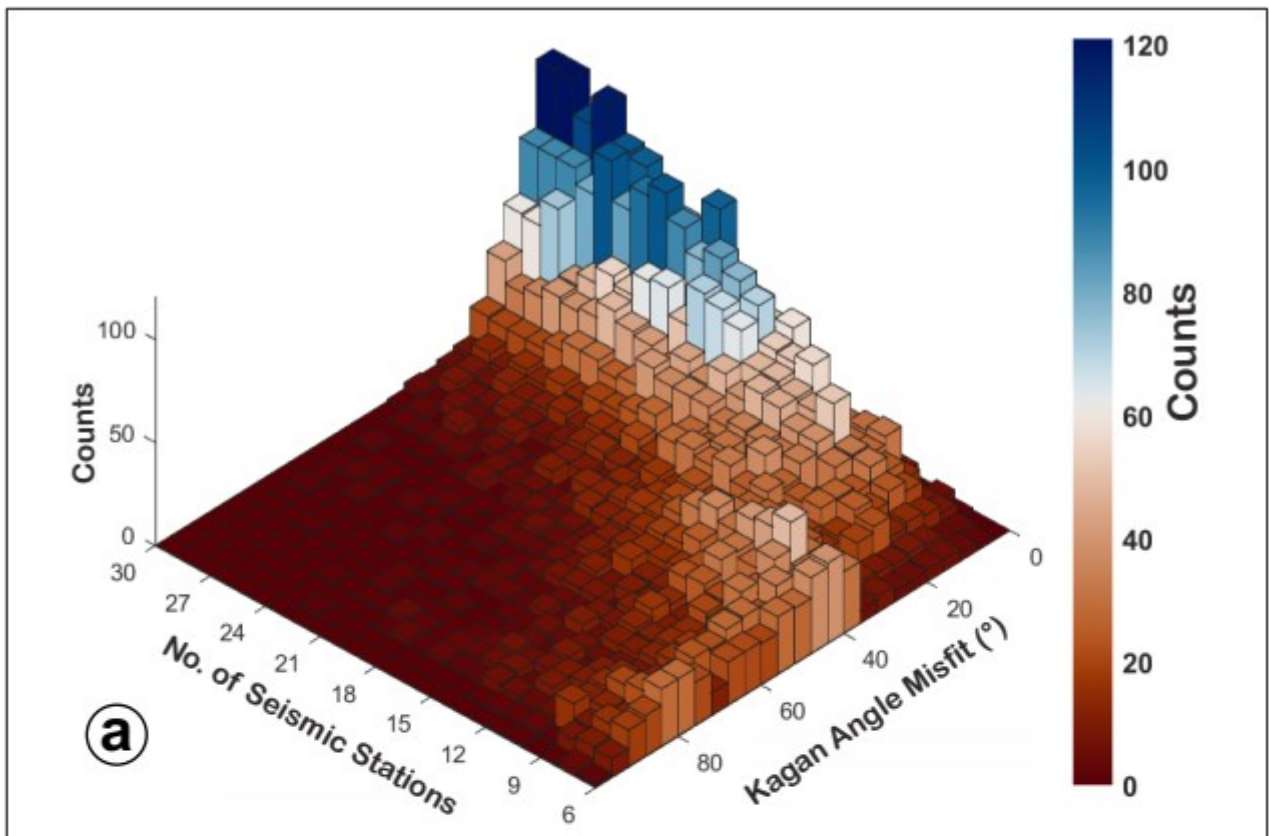
Figure 13. 3D-histograms of the test results in terms of number of stations (a), azimuthal gap (b) and KA misfit. The simulations were carried out with a free network configuration.